Supplementary Figure 1

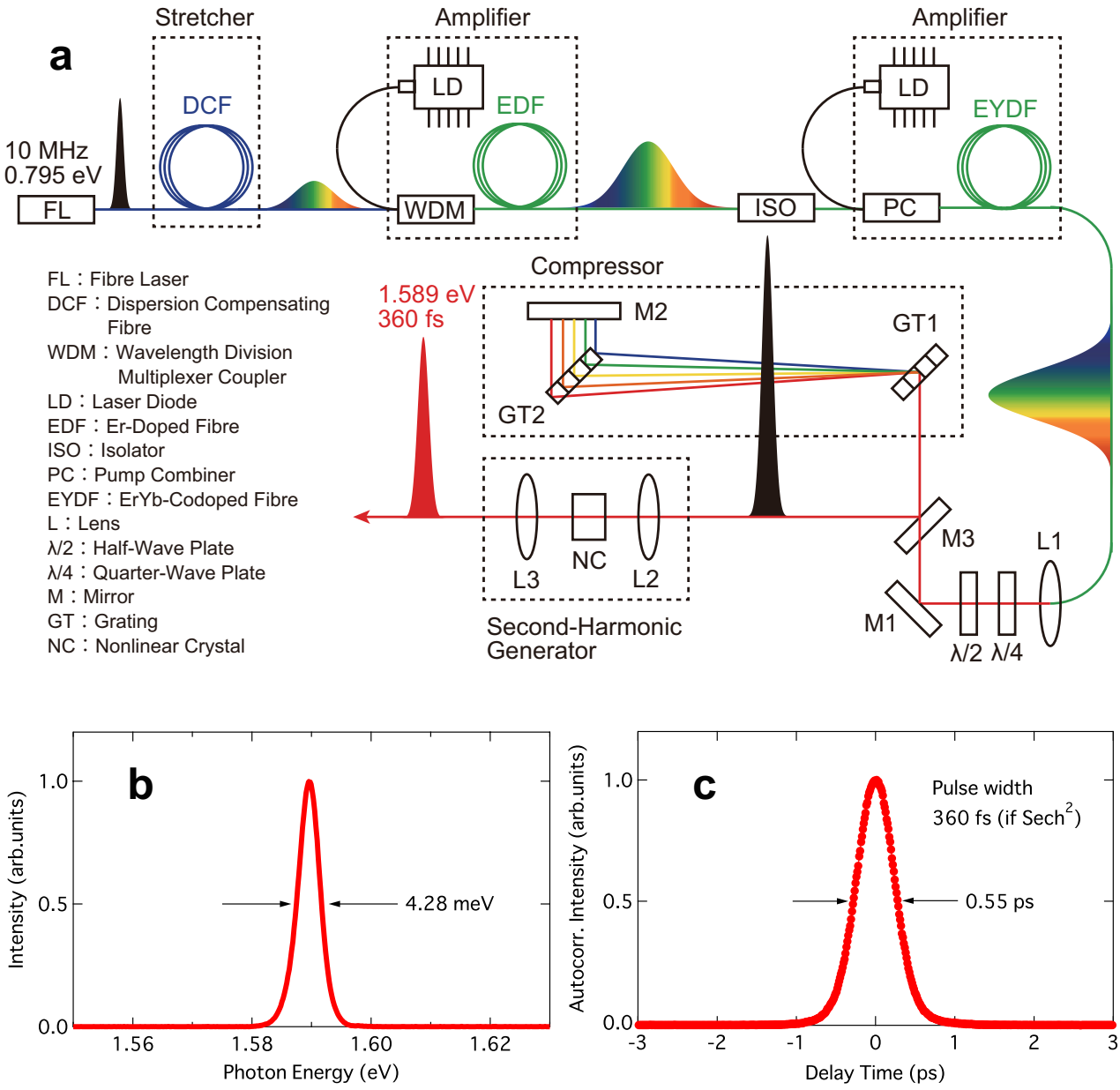

Supplementary Figure 1| Fibre laser system. a, Schematic of the CPA configuration of the developed 10-MHz-repetition-rate ML fibre laser system. **b**, Energy spectrum and **c**, autocorrelation function for the output pulses.

Supplementary Figure 2

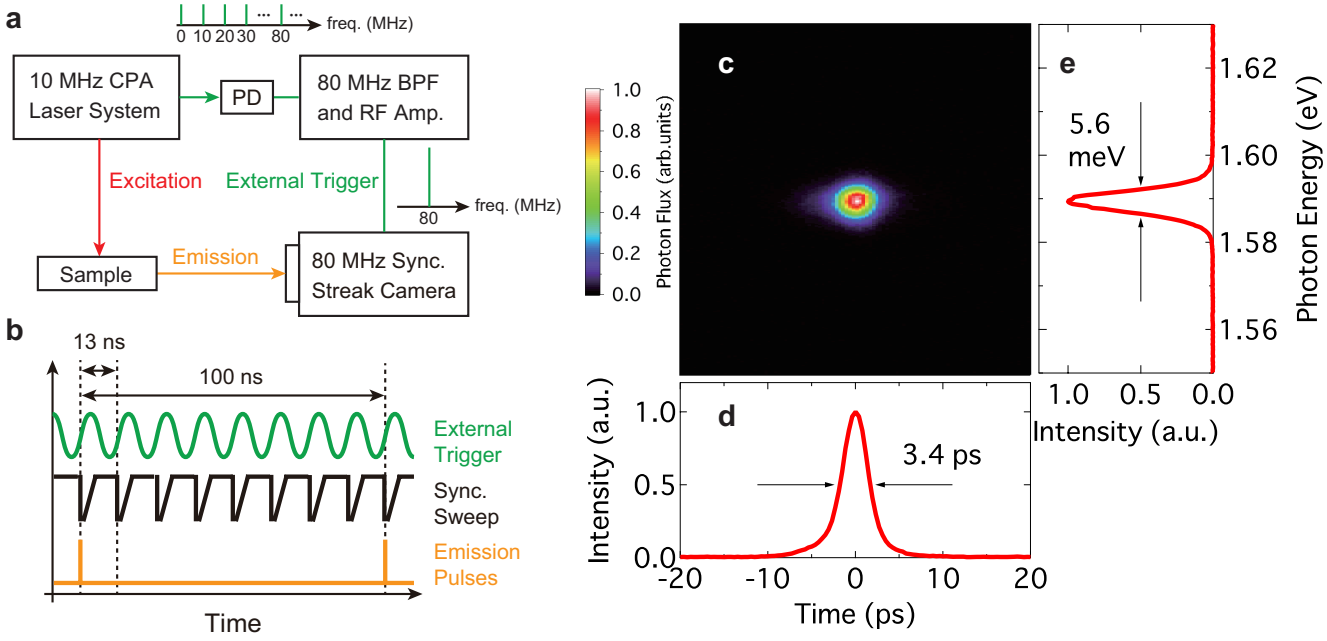

Supplementary Figure 2| Measurement system. a, Schematic of the time- and energy-resolved measurement system of the 10-MHz-repetition-rate fibre laser system combined with an 80 MHz synchronous-scan-mode streak camera. **b**, Timing chart of the measurement system. **c**, Time- and energy-resolved observation of the output from the fibre laser system. **d–e**, Energy-integrated time waveform and time-integrated energy spectrum for Supplementary Figure 2**c**, respectively.

Supplementary Figure 3

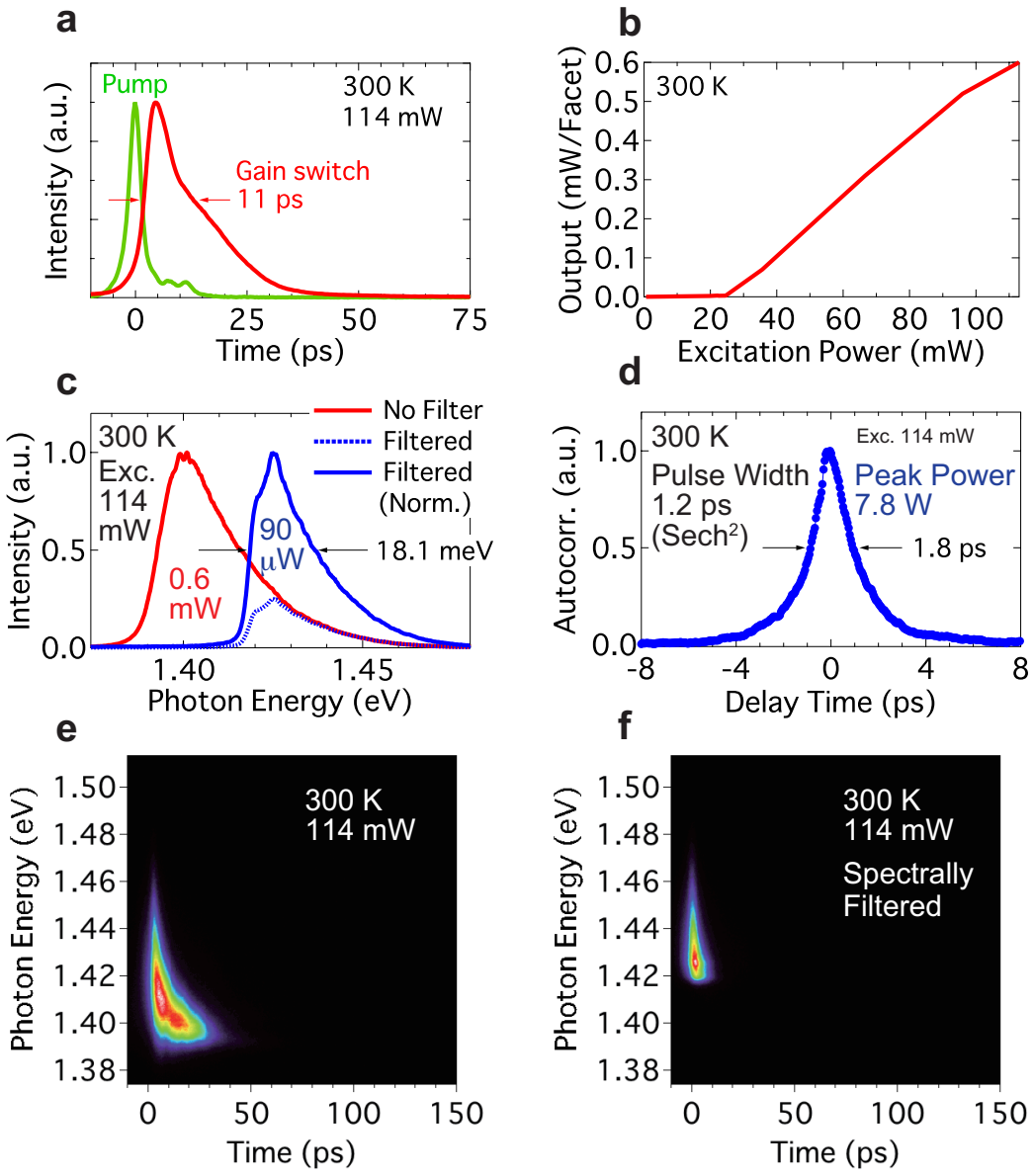

Supplementary Figure 3| Experimental results at sample temperature of 300 K. a, Time-resolved spectrally integrated waveform represented as a red curve with an excitation power of 114 mW, where the green curve is the excitation pulse. **b**, Average output power depending on the excitation power. **c,** Time-integrated energy spectrum, where the red and blue curves represent the full and spectrally filtered energy spectra above 1.415 eV of the gain-switched pulses with an excitation of 114 mW, respectively. **d,** Autocorrelation function of the spectrally filtered gain-switched pulses with excitation power of 114 mW. **e,** Time-resolved full spectral emission. **f,** Time-resolved spectrally filtered emission, where the high-energy component is extracted above 1.415 eV by a high-pass filter.

Supplementary Figure 4

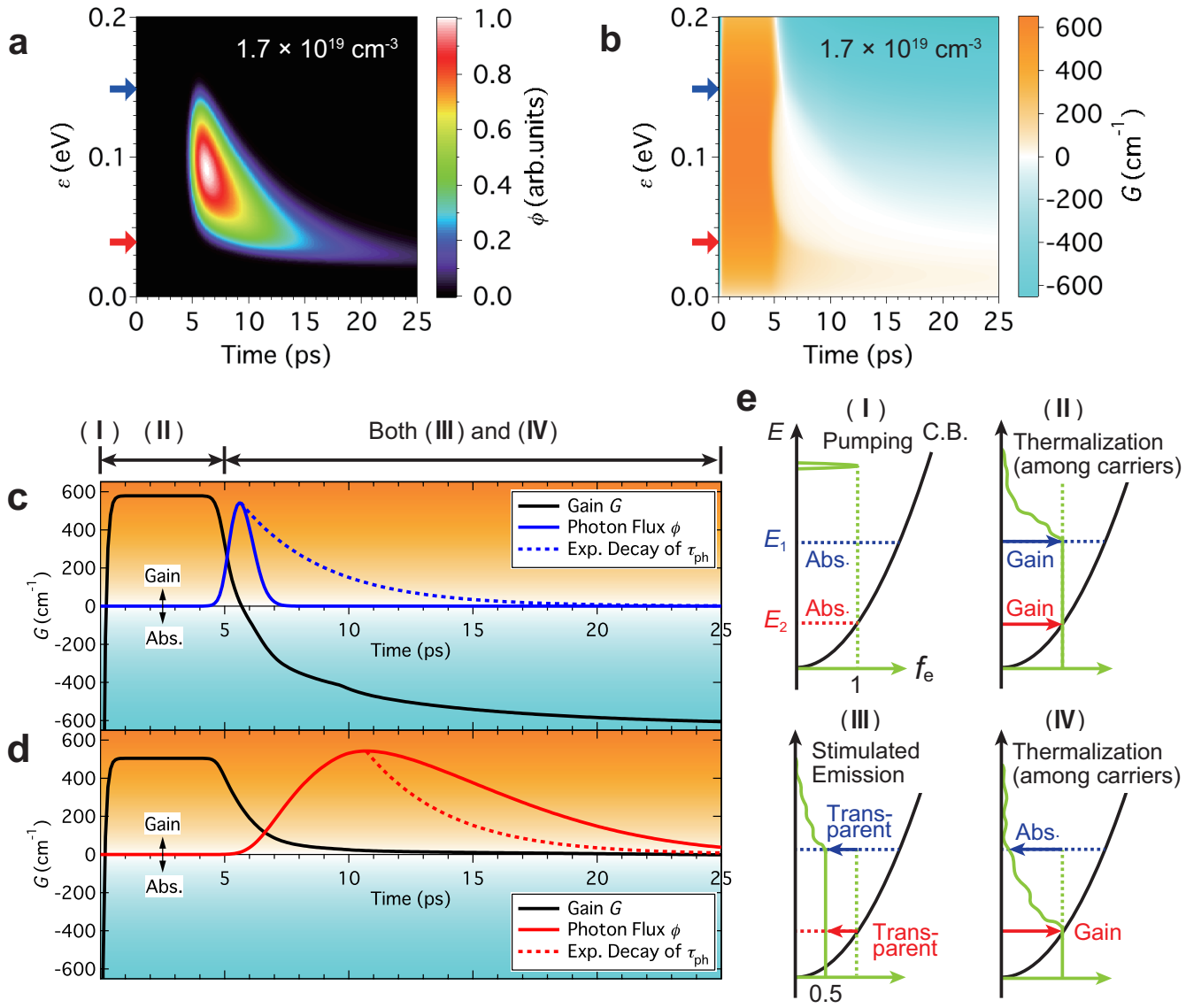

Supplementary Figure 4| Simulated pulse dynamics and interpretation. a, Calculated spectral dynamics of the photon flux ϕ and **b**, gain G with the initial carrier density of 1.7×10^{19} cm^{-3}. **c–d**, Time profiles of the solid blue and red curves in Supplementary Figure 4**a** at ε = 0.149 eV (blue arrow) and ε = 0.040 eV (red arrow), respectively. Therein, the dotted curves are exponential functions of the decay constant τ_{ph} = 3.4 ps. The black solid curves are time profiles of the gain G at the two energy levels in Supplementary Figure 4**b**. **e**, Schematic dynamical energy distribution functions of electrons f_e in the conduction band divided into four regimes from (I) to (IV).

Supplementary Table 1

Supplementary Table 1| Summary of the output pulses at sample temperature of 5 K and 300 K with spectral filtering. The excitation powers are 94 mW and 114 mW at 5 K and 300 K, respectively. In both temperature conditions, the pulse widths are significantly shorter than the cavity lifetime of 3.4 ps and peak powers are more than 7 W.

Sample temperature (K)	5	300
Excitation power (mW)	94	114
Pulse width (ps)	0.67	1.2
Average power (μW)	50	90
Pulse energy (pJ)	5	9
Peak power (W)	7.5	7.8
Central wavelength	1.53 eV (810 nm)	1.43 eV (870 nm)
Spectral width	12.1 meV (6.4 nm, 2.9 THz)	18.1 meV (11 nm, 4.4 THz)
Time bandwidth product	1.9	5.1

Supplementary Table 2

Supplementary Table 2| Summary of the characterization of the fibre laser system in comparison with a conventional ML Ti:Sapphire oscillator.

	Second harmonics	Fundamental waves	Conventional ML Ti:Sa oscillator
Max. average power (W)	0.33	0.61	1.0
Repetition rate (MHz)	10	10	80
Pulse energy (nJ)	33	61	12
Pulse width (ps)	360	450	200
Peak power (kW)	90	140	60
Central wavelength	1.589 eV (780 nm)	0.795 eV (1560 nm)	1.589 eV (780 nm)
Spectral width	4.28 meV (2.1 nm, 1.03 THz)	5.34 meV (10.5 nm, 1.29 THz)	6.5 meV (3.2 nm, 1.6 THz)
Time bandwidth product	0.37	0.58	0.32

Supplementary Note 1

Supplementary Figure 3a presents the spectrally integrated time waveforms of the gain-switched pulses including full spectral emission at a sample temperature of 300 K with an excitation power of 114 mW. Herein, the red and green curves represent the time waveform of the emission and pump pulses scattered at the sample edge, respectively. The pulse width at 300 K is 11 ps to be broader than that of 7 ps at 5 K shown in Fig. 2b.

Supplementary Figure 3b illustrates the dependence of the average output power on the excitation power at the sample temperature of 300 K. The lasing threshold at 300 K is 25 mW to be higher than that of 0.9 mW at 5 K presented in Fig. 2c. The average output power is 0.6 mW at 300 K with an excitation power of 114 mW, which is lower than that of 2.4 mW at 5 K with an excitation power of 94 mW.

Supplementary Figure 3c presents the time-integrated spectrally resolved spectra under an excitation power of 114 mW at 300 K. The red curve represents the full spectral emission, where the centre of mass of the spectrum is 1.40 eV. The blue dotted curve represents the spectrally filtered spectrum extracted above 1.415 eV from the red curve by a high-pass filter, which reduced the average power in the spectrum from 0.6 mW to 90 μW. The solid blue curve shows the normalised spectrum with the spectral width of 18.1 meV.

Supplementary Figure 3d shows the intensity-autocorrelation function after the spectral filtering at 300 K at the excitation power of 114 mW. The FWHM is 1.8 ps, corresponding to a pulse width of 1.2 ps estimated from the sech^2 of the pulse shape on the time waveform. The pulse width at 300 K is also significantly shorter than the cavity lifetime of 3.4 ps. The peak power of the pulses is achieved as 7.8 W.

Supplementary Figure 3e shows time-resolved full spectral dynamics of the gain-switched pulses at the excitation power of 114 mW, measured using the synchronous-scan-mode streak camera with a time and energy resolution of 3 ps and 3 meV, respectively. As for the high-energy region, the time duration is limited by the measurement system. The spectral filtering extracted the spectrum above 1.415 eV, as shown in Supplementary Figure 3f. As a result, it can be seen the pulse width is 1.2 ps via the autocorrelation measurement after the spectral filtering. Meanwhile, the pulse width of the low-energy components at 1.40 eV is 20-ps longer than the cavity lifetime of 3.4 ps. The gain switching at 300 K exhibits common pulse dynamics at 5 K in terms of the fact that the high- and low-energy components are far shorter and longer than the cavity lifetime, respectively.

Supplementary Note 2

Our multi-mode laser rate equations with a non-equilibrium carrier energy distribution f_α at an energy ε and time t can be given by

$$\frac{\mathrm{d}f_\alpha(\varepsilon,t)}{\mathrm{d}t} = f_\alpha^{\mathrm{cf}}\delta(\varepsilon-\varepsilon_{\mathrm{ex}},t) - \frac{f_\alpha(\varepsilon,t) - f_\alpha^{\mathrm{th}}\big(\varepsilon,T(t),\mu_\alpha(t)\big)}{\tau_{\mathrm{r}}} - \frac{v_{\mathrm{g}}G(\varepsilon,t)\phi(\varepsilon,t)}{D(\varepsilon)}, \qquad \alpha = \mathrm{e,h} \quad \text{(S1)}$$

$$\frac{\mathrm{d}\phi(\varepsilon,t)}{\mathrm{d}t} = v_{\mathrm{g}}G(\varepsilon,t)\phi(\varepsilon,t) - \frac{\phi(\varepsilon,t)}{\tau_{\mathrm{ph}}}. \quad \text{(S2)}$$

For simplicity, we switched off the relaxation or cooling via phonon emission and tested minimal calculations with the multi-mode laser rate equations including only the carrier–carrier scattering mechanism, where carriers thermalize among themselves within a few hundred femtoseconds but are not cooled via the emission of energy (heat) to the lattice[1]. Surprisingly, such a simple calculation with appropriately chosen parameters successfully reproduced and clarified the short pulse generation beyond the photon-lifetime limit.

In Eq. (S1), the first term represents impulsive pumping carriers into the energy band at $\varepsilon_{\mathrm{ex}}$, which is described by a Dirac delta function with coefficients of f^{cf}_α. The second term represents the thermalization of f_α towards the thermal distributions f^{th}_α via intraband relaxation due to carrier–carrier scattering in the time constant τ_{r}. f^{th}_α are treated as Fermi distribution functions in which the carrier temperature T and chemical potentials μ_α are determined on the condition that the interaction between carriers and phonons is neglected. Thus, the population n_α and total kinetic energy of the electron–hole system $u_{\mathrm{e}} + u_{\mathrm{h}}$ conserved before and after thermalization are

$$n_\alpha(t) = n_\alpha^{\mathrm{th}}(t), \quad \text{(S3)}$$

$$u_{\mathrm{e}}(t) + u_{\mathrm{h}}(t) = u_{\mathrm{e}}^{\mathrm{th}}(t) + u_{\mathrm{h}}^{\mathrm{th}}(t). \quad \text{(S4)}$$

For instance, $T(0) = 1000$ K, $\mu_{\mathrm{e}}(0) = 0.34$ eV, and $\mu_{\mathrm{h}}(0) = -0.10$ eV are obtained with the initial carrier density of 1.7×10^{19} cm^{-3} and $\varepsilon_{\mathrm{ex}} = 0.4$ eV. The third term in Eq. (S1) represents the stimulated recombination depending on

the group velocity v_g, gain coefficient $G \propto f_e + f_h - 1$, photon flux ϕ, and joint density of states D. In Eq. (S2), τ_{ph} is the photon lifetime. The parameters are τ_r = 100 fs, τ_{ph} = 3.4 ps, v_g = 73 μm/ps, and ε_{ex} = 0.4 eV in this simulation. Numerical results with physical interpretations are provided in Supplementary Note 3.

To interpret the observed phenomena, we can reference an early experiment[2]. They reported picosecond gain-switched pulses with a high-energy component of a shorter width and delay than the low-energy component, suggesting the contribution of ultrafast intraband carrier relaxation. Indeed, they modelled gain-switched lasing in the presence of ultrafast carrier relaxation or cooling due to the optical-phonon-emission mechanism and performed numerical simulations with multi-mode laser rate equations to explain their observed results. However, significantly shorter pulses than the photon lifetime in our experiment are unexplained in this model, so we searched for a new mechanism.

Supplementary Note 3

Supplementary Figure 4a presents the spectral dynamics of the photon flux ϕ with the initial carrier density of 1.7×10^{19} cm^{-3} calculated by Eqs. (S1–S4) in Supplementary Note 2. The duration and delay of the higher-energy component, e.g., at ε = 0.149 eV, indicated by a blue arrow in the pulse spectrum, is shorter than that of the lower-energy component at ε = 0.040 eV, indicated by a red arrow. Supplementary Figures 4c and d describe the time profiles of Supplementary Figure 4a, where the solid blue and red curves represent those at ε = 0.149 and 0.040 eV, respectively. Therein, the dotted curves represent the exponential decay functions with a time constant of 3.4 ps, corresponding to the photon lifetime in the cavity. The pulse width of the blue curve is 1.1 ps, which is far shorter than the photon lifetime. The pulse width of the red curve is 14 ps. The present simulation successfully reproduces the experimental features of the photon energy dependence.

To investigate the origin of the short pulses, in Supplementary Figures 4c and d, the black curves represent the spectral dynamics of the gain G in Supplementary Figure 4b calculated with the initial carrier density of 1.7×10^{19} cm^{-3} and time profiles at ε = 0.149 and 0.040 eV, respectively, where the background colours are the same colour scale as in Supplementary Figure 4b. Regarding Supplementary Figure 4d after impulsive pumping, the gain increases towards a saturated level ($G > 0$, orange) in less than a picosecond and remains constant at 500 cm^{-1} until t = 4.5 ps. Subsequently, the gain decreases slowly to transparency (G = 0, white) in picoseconds. In contrast,

the saturation gain of 580 cm^{-1} in Supplementary Figure 4c switches rapidly through the intersection for $G = 0$ at $t = 5.7$ ps to absorption ($G < 0$, cyan), which extinguishes photons in the cavity. Therefore, the decay time becomes shorter than τ_{ph} and the pulse width can surpass the photon-lifetime limit.

To understand the mechanisms that rapidly switch G from gain to absorption only at the high energy $\varepsilon = 0.149$ eV, our interpretation is illustrated in Supplementary Figure 4e associated with Supplementary Figures 4c–d, where we virtually divide the carrier dynamics into four regimes from (I) to (IV). In regime (I), the high-density carriers are excited into the active layer by an impulsive intense pulse at $t = 0$. In regime (II), ultrafast intraband thermalization among the carriers due to carrier–carrier scattering spreads the excited carriers in the energy bands and induces extremely-high-density population inversion ($f_e \sim f_h \sim 1$), covering the energy levels of E_1 and E_2 within $t = 0.5$ ps. The gain saturates to 580 cm^{-1} at E_1 and 500 cm^{-1} at E_2 and initiates the gain-switched operation. The optical density in the cavity still remains at a low level. In regime (III), significant stimulated emission increases the optical density, where the time constant of the rise is inversely proportional to the saturation gain at the energy levels[3]. The emission occurs rapidly, e.g., within $t = 5.7$ ps at E_1, and consumes a significant number of carriers in the energy bands, which is just the typical gain switching operation. Note here that the gain switching reduces the carrier population only to the transparent density ($f_e \sim f_h \sim 0.5$) and, therefore, the pulse width is limited by the photon lifetime just as the conventional rate equations shown in Fig. 1a. In regime (IV), when the stimulated emission decreases the carrier distribution to 0.5, the intraband thermalization induces G to change from transparency to absorption ($f_e \sim f_h \sim 0$) at E_1, whereas, at E_2, G changes in the opposite direction from transparency to gain ($f_e \sim f_h \sim 1$). In reality, (III) and (IV) occur simultaneously and repeatedly. As a result, G changes rapidly from gain to absorption at the high-energy region $\varepsilon = 0.149$ eV and slowly from gain to transparency at the low-energy region $\varepsilon = 0.040$ eV.

Supplementary References

[1] Shah, J. *Hot carriers in semiconductor nanostructures: physics and applications, 1st edition*. Chap. IV (Academic Press, San Diego, 1992).

[2] Koch, T., Chu, L., Harder, Ch. & Yariv, A. Picosecond carrier dynamics and laser action in optically pumped buried heterostructure lasers. *Appl. Phys. Lett*. **41**, 6 (1982).

[3] Ito, T. *et al*. Transient hot-carrier optical gain in a gain-switched semiconductor laser. *Appl. Phys. Lett*. **103**, 082117 (2013).